Revealing a High Water Abundance in the Upper Mesosphere of Mars with ACS onboard TGO

Denis A. Belyaev[1,1], Anna A. Fedorova[2,2], Alexander Trokhimovskiy[1,1], Juan Alday Parejo[3,3], Franck Montmessin[4,4], Oleg I Korablev[1,1], Franck Lefèvre[5,5], Andrey Patrakeev[2,2], Kevin S. Olsen[3,3], and Alexey V. Shakun[1,1]

[1]Space Research Institute (IKI)
[2]Space Research Institute
[3]University of Oxford
[4]LATMOS CNRS/UVSQ/IPSL
[5]LATMOS

November 30, 2022

Abstract

We present the first water vapor profiles encompassing the upper mesosphere of Mars, 100–120 km, far exceeding the maximum altitudes where remote sensing has been able to observe water to date. Our results are based on solar occultation measurements by Atmospheric Chemistry Suite (ACS) onboard the ExoMars Trace Gas Orbiter (TGO). The observed wavelength range around 2.7 µm possesses strong CO2 and H2O absorption lines allowing sensitive temperature and density retrievals. We report a maximum H2O mixing ratio varying from 10 to 50 ppmv at 100–120 km during the global dust storm (GDS) of Martian Year (MY) 34 and around southern summer solstice of MY 34 and 35. During other seasons water remains persistently below ~2 ppmv. We claim that contributions of the MY34 GDS and perihelion periods into the projected hydrogen escape from Mars are nearly equivalent.

Posted on 30 Nov 2022 — CC-BY-NC 4 — https://doi.org/10.1002/essoar.10506560/v2 — This a preprint and has not been peer reviewed. Data may be preliminary.

Revealing a High Water Abundance in the Upper Mesosphere of Mars with ACS onboard TGO

Denis A. Belyaev[1], Anna A. Fedorova[1], Alexander Trokhimovskiy[1], Juan Alday[2], Franck Montmessin[3], Oleg I. Korablev[1], Franck Lefèvre[3], Andrey S. Patrakeev[1], Kevin S. Olsen[2], and Alexey V. Shakun[1]

[1]Space Research Institute (IKI), Moscow, Russia.

[2]Department of Physics, University of Oxford, UK.

[3]LATMOS/CNRS, Paris, France.

Corresponding author: Denis Belyaev (dbelyaev@iki.rssi.ru)

Key Points:

- Water abundances are reported in a previously unexplored altitude range: from 100 to 120 km
- The observed GDS (MY34) and two perihelion seasons (MY34, 35) reveal the H2O content around 10-50 parts per million by volume at 100-120 km
- Contributions of the MY34 GDS and perihelion periods into the projected hydrogen escape from Mars are nearly equivalent

Abstract

We present the first water vapor profiles encompassing the upper mesosphere of Mars, 100–120 km, far exceeding the maximum altitudes where remote sensing has been able to observe water to date. Our results are based on solar occultation measurements by Atmospheric Chemistry Suite (ACS) onboard the ExoMars Trace Gas Orbiter (TGO). The observed wavelength range around 2.7 μm possesses strong CO_2 and H_2O absorption lines allowing sensitive temperature and density retrievals. We report a maximum H_2O mixing ratio varying from 10 to 50 ppmv at 100–120 km during the global dust storm (GDS) of Martian Year (MY) 34 and around southern summer solstice of MY 34 and 35. During other seasons water remains persistently below ~2 ppmv. We claim that contributions of the MY34 GDS and perihelion periods into the projected hydrogen escape from Mars are nearly equivalent.

Plain Language Summary

We report regular events of high abundances of the water vapor (H_2O) in the upper atmosphere of Mars (100–120 km). So far, any water enrichment has not been revealed by remote sensing at such high altitudes. Higher than 80 km, solar light breaks water vapor molecules into H and O atoms, which may reach the exosphere and escape the planet. When Mars is closer to the Sun (the perihelion season), the atmosphere's circulation intensifies, causing increased dust activity with global dust storms (GDS), occurring every 3–4 Mars years. We observed during the second halves of Martian years 34 and 35 (2018–2020), including one GDS and two perihelion seasons. We report that the maximum water relative abundance reaches 10–50 parts per million in volume (ppmv) at 100-120 km during the GDS and every perihelion season. These high values indicate that the Martian atmosphere above 100 km regularly hosts large amounts of water, facilitating the long-term escape of water from the planet.

1 Introduction

The vertical distribution of water vapor (H_2O) on Mars is an indicator of the intricate coupling of distinct phenomena: temperature variations, cloud formation, sublimation, turbulent and convective mixing, as well as general circulation and wave/eddy transport. H_2O has long been thought to remain confined below the hygropause, which is the level where the saturation condition is met and where water ice clouds may form, as occurs on Earth. The existence of this layer on Mars was established for the first time by ground-based microwave soundings of Clancy et al. (1996) with a saturation level between 10–20 km around the aphelion, i.e., Solar Longitudes (L_S) 70°, and 40–60 km around perihelion (L_S 250°). In parallel, Rodin et al. (1997) reported water vapor profiles retrieved from the solar occultations made by Auguste on Phobos-2 in 1989. The existence of a hygropause at 30–35 km (with a mixing ratio of 3 ppm) in the northern spring (L_S=0°–20°) near the equator was subsequently claimed. The first climatology of water vapor profiles was derived from SPICAM-IR solar occultations on Mars Express (MEx) (Fedorova et al., 2009; 2018; 2021; Maltagliati et al., 2013), covering eight Martian years. The hygropause level was found to vary from 40 to 80 km depending on season, latitude, and dust events. Hygropause is also indirectly sensed in CRISM limb profiles of $O_2(^1\Delta g)$ emission, a confident indicator of O_3, from which water vapor mixing ratios were inferred by Clancy et al. (2017).

The observation of large amounts of water vapor in and above the middle atmosphere (>40 km, Maltagliati et al., 2013) was then complemented by the discovery of short-term decline of the hydrogen corona brightness over several weeks (Chaffin et al., 2014; Clarke et al., 2014). This variability exposed a new paradigm in our perception of how water escapes from Mars (Chaffin et al., 2017). So far, water escape was thought to be controlled by a slow conversion process involving H_2, formed from the catalytic recombination of carbon dioxide with odd hydrogen (McElroy and Donahue, 1972; Krasnopolsky, 2002). The non-condensable H_2 can overcome the hygropause and reach the mesosphere (80–120 km), while transported by turbulent mixing or circulation. There, it can dissociate and release H atoms that will escape the planet once above the exobase.

Observations have revealed that water vapor transport from the troposphere to the lower mesosphere of Mars occurs during the dusty season and is enhanced at times of major dust storms. In particular, a significant H_2O enhancement in the middle atmosphere was observed during the global dust storm (GDS) in 2007 (MY28) with a rise of the hygropause altitude to >60 km (Fedorova et al., 2018; Heavens et al., 2018; 2019). Sensitive solar occultation measurements by NOMAD and ACS NIR instruments onboard the ExoMars Trace Gas Orbiter (TGO) have showed that water vapor reached 80–100 km (Aoki et al., 2019; Fedorova et al., 2020) during two storms in 2018 and 2019 (a global one at L_S 190°–220° and a regional one at L_S 330° in MY34; Montabone et al., 2020). Fedorova et al. (2020) revealed the water supersaturation at 70–90 km even in the presence of H_2O ice clouds not only during the GDS but also near the Southern summer solstice (L_S~270°) when water reached 90-100 km as well. Altogether, these studies promote a new mechanism for controlling H escape through direct delivery at above 80 km and further photodissociation of H_2O molecules (Chaffin et al., 2017; Krasnopolsky et al., 2019). General circulation models predict an upward water flux into the thermosphere (>120 km) during the GDS and perihelion periods (Shaposhnikov et al., 2019; Neary et al., 2020; Rossi et al. 2021).

The discussion regarding a relative contribution of perihelion or GDS to the mesospheric water enrichment was recently stimulated by SPICAM/MEx long-term observations covering Martian Years 28 through 35. Here, Fedorova et al. (2021) claimed an annual rise of water abundance up to ~90 km in perihelion, which is compatible with GDS enhancements. The new ACS/TGO dataset confirms those conclusions for altitudes below 100 km in MY34–MY35 (Fedorova et al. 2020, Alday et al., 2021). In parallel, during the perihelion season, the D/H ratio in water decreases with altitude from 4–6 times SMOW (Standard Mean Ocean Water) in the lower atmosphere to 2–3 times in the mesosphere (50-70 km) as measured by ACS MIR (Alday et al., 2021) and NOMAD (Villanueva et al., 2021) spectrometers. Alday et al. (2021) show that ultraviolet H_2O photolysis dominates the production of H relative to D atoms in the upper atmosphere.

From above, ion chemistry in the thermosphere has been characterized by the NGIMS mass-spectrometer on MAVEN (Benna et al., 2015) and interpreted by the ionospheric model of Fox et al. (2015). Using NGIMS data, Stone et al. (2020) measured H_2O ion concentrations around ~150 km for the 2014–2018 period (MY32–MY34). With the help of the model by Fox et al. (2015), Stone et al. (2020) found the relative abundance of water at this altitude on the dayside varying seasonally on average from 2 to 5 ppm. Several enhanced dusty episodes disrupt this seasonal signal: 3–9 ppm during the regional storm of MY32, 10–20 ppm during the storm of MY33, and up to 60 ppm in the GDS of MY34. Stone et al. (2020) concluded that water transport into the ionosphere and its destruction are the main mechanisms in the overall hydrogen escape from Mars.

We used the data of the middle infrared spectrometer of the Atmospheric Chemistry Suite (ACS MIR) onboard the ExoMars TGO, which measures water vapor VMR and atmospheric density in a wide range of altitudes, from the troposphere to the lower thermosphere, using the strong absorption bands of H_2O and CO_2 around 2.66–2.70 µm. The high spectral resolution and the good signal-to-noise ratio of ACS MIR allow the measurements of water profiles up to 120 km, inaccessible altitudes for the ACS NIR and SPICAM measurements, sensing the 1.38 µm absorption band (Fedorova et al., 2020; 2021). The strong H_2O absorption around 2.6 µm is also used by NOMAD, yielding water profiles up to ~90 km (Aoki et al., 2019; Villanueva et al., 2021).

Here we report the first water vapor abundance measurements in the upper mesosphere (up to 120 km) of Mars. The goal of our paper is to compare the mesospheric water behavior between the second halves of MY34 and MY35 when the high H_2O content is observed. We aim to clarify the principal mechanism of H_2O delivery to the upper mesosphere: it is sporadic dust events, or the result of seasonal variability in the Martian circulation that peaks each year, around Southern summer solstice. For that, we analyze seasonal and latitudinal variations of H_2O VMR vertical profiles retrieved from the ACS MIR solar occultation experiment.

2 Measurements and dataset overview

2.1 ACS MIR spectroscopy and retrievals

ACS MIR, a solar occultation cross-dispersion echelle spectrometer, records spectra from a set of adjacent diffraction orders (from 10 to 20 per occultation) projected onto a 2D detector array (Korablev et al., 2018). To retrieve high altitude water vapor abundances together with the atmospheric temperature and pressure, we use MIR spectra from the diffraction order #223. They cover a narrow wavelength interval of 2.66–2.68 µm (3733–3753 cm^{-1}), including a part of the 2.7-µm CO_2 absorption band and a few strong H_2O lines near 2.66 µm (Fig. 1a, 1b, Fig. S1). The instrument's spectral resolution is ~0.15 cm^{-1}, while the signal-to-noise ratio ranges from 2,000 to 4,000, which provides high sensitivity for detections in the upper atmosphere where atmospheric constituent densities are low. Temperature (Fig. 1c) is retrieved by fitting a synthetic model to the CO_2 rotational band taking advantage of its temperature dependence as seen in Fig. S1 of the Supplementary Material (SM). This procedure was applied iteratively, with the pressure calculated from the retrieved temperature profile under the assumption of hydrostatic equilibrium. The temperature measurements were then validated against those made by MIR near the 2.6 µm CO_2 band (Alday et al., 2019) and by ACS NIR around the 1.58 µm band (Fedorova et al., 2020). As a result, one occultation session allows us to simultaneously retrieve profiles of pressure and temperature (from CO_2 absorption bands) and the H_2O number density (Fig. 2c). The water abundance can then be expressed relative to the total atmospheric density, that is, in VMR (in ppmv). Specific details of the algorithms pertaining to this work can be found in SM.

The dataset analyzed here consists of a series of transmission spectra obtained during a solar occultation while the line of sight of the instrument progressively penetrates from the upper into deeper layers of the atmosphere, or vice versa (see examples in Fig. 1a, 1b). The transmission is determined as the solar spectrum ratio measured through the atmosphere to the reference one, taken from the data above a tangent height of 200 km. This altitude level is negligibly attenuated by the atmosphere even within the very strong CO_2 band system at 2.7 µm.

The typical integration time is 2 seconds, which provides an altitude resolution ranging from 0.5 to 2.5 km, depending on the occultation duration. It gives sufficiently fine vertical sampling for an atmosphere whose scale height ranges from 5 to 10 km depending on temperature. The instrument field of view projected at the limb is around 1-3 km in altitude equivalent.

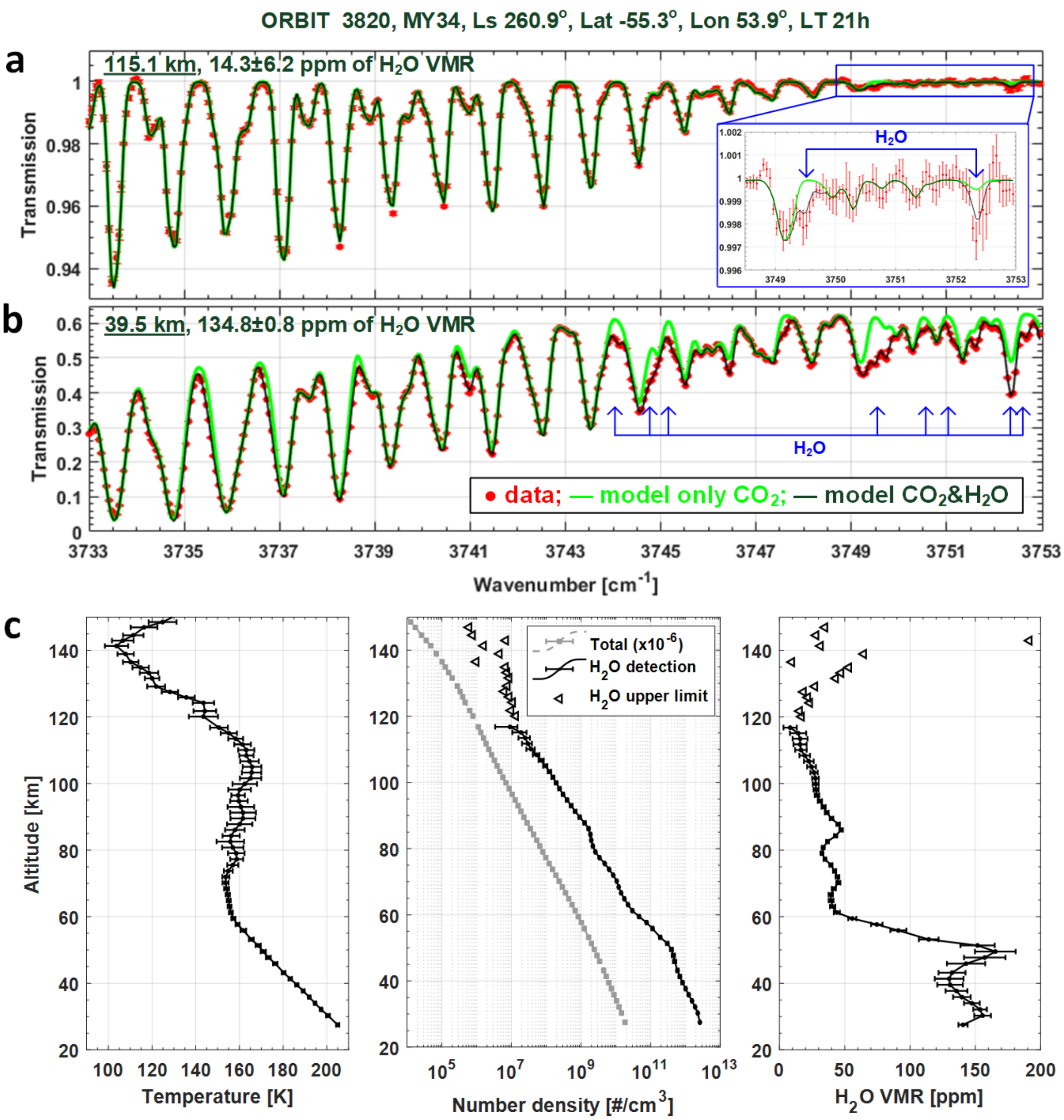

Figure 1. Example ACS MIR spectra and profiles of the retrieved quantities. Measured transmission spectra (red) at tangent altitudes of 115.1 km (**a**) and 39.5 km (**b**) are compared with the best-fit models, including both CO_2 and H_2O absorptions (black), and only CO_2 absorption (green). Blue arrows indicate water absorption lines. Zoom in (**a**) shows a part with the strongest H_2O absorption detected at 115 km. (**c**) Retrieved vertical profiles of temperature (left), number densities (center), and H_2O volume mixing ratio (VMR) (right). The atmospheric

density (grey squares) is scaled by the factor of 10^{-6}. Black triangles mark H_2O upper limits (see SM for the description of uncertainties).

2.2 Data selection

Our measurements of the mesospheric water focus on the second halves of MY34 and MY35, which correspond to ACS MIR observations from May 2018 to March 2019 and from April 2020 to January 2021. The selected dataset comprises 187 occultation sessions in the Northern Hemisphere and 156 sessions in the Southern Hemisphere, encompassing seasonal periods from L_S 180° to 355° in MY34 and from L_S 185° to 356° in MY35 (Fig. 2a). Figure 2a shows the latitude coverage with the corresponding aerosol activity, which was defined for each occultation at the altitude level where the slant opacity equals 0.3 (~0.75 of the atmospheric transmittance in the continuum). Measurements in the Northern Hemisphere occurred mostly in the high latitude range, between 40°N and 70°N. In the South, the perihelion observations (L_S 270°) were made in mid-latitudes, while the rest of occultations occurred close to the polar region (60°S–90°S). Only a few sessions were localized nearby the equator: at L_S~240° and L_S~300° of MY34 and at L_S~210° and L_S~280° of MY35. These observations are accompanied by a higher aerosol loading than for high latitude and polar regions (Fig. 2a).

3 Seasonal variation of altitude profiles

Observations in the second halves of MY34 and MY35 uncover events, which drastically perturbed the temperature and water vapor vertical distributions. The peculiar pattern to compare with is the MY34 GDS and perihelion periods in MY34 versus MY35, which had no GDS but a regional dust activity in its second half. The seasonal variation of the processed altitude profiles is presented in Figure 2(b, c). We binned the profiles into intervals of 2° in solar longitude and 2 km in altitude. Depending on the L_S and altitude sampling, the value in each bin is calculated as the weighted mean of one to five individual points. We excluded all points with 1-sigma uncertainties exceeding 20 K in temperature and 100% of the H_2O mixing ratio. The second rejection criterion corresponds to the detection limit (~10^7 cm^{-3}) of water number density (see in Fig. 1c) that defines the seasonal variations of the uppermost detectable points in Figure 2c.

We observe seasonal temperature (Fig. 2b) and H_2O (Fig. 2c) peaks in the middle atmosphere (40–80 km) during the GDS of MY34, L_S 190°–220°, and an additional smaller peak at L_S 320°–330°, corresponding to a regional storm. Moreover, the rise of water vapor to higher altitudes, up to the mesopause at 110–130 km where temperature encounters a minimum, is observed during the two perihelion intervals (L_S 250°–290°) of MY34 and MY35. Here, the Southern summer (Fig. 2c, right panel) is accompanied by a more humid mesosphere (40–60 ppm of H_2O) than the Northern Winter (Fig. 2c, left panel) where the mean mesospheric water reaches 20–30 ppmv on average between 80 and 120 km. In contrast, out of the perihelion peak or dust events, i.e. for the selected data at the beginning of the MY34 GDS and at the very end of MY 34, 35, water content above 80 km never exceeds 2-3 ppmv.

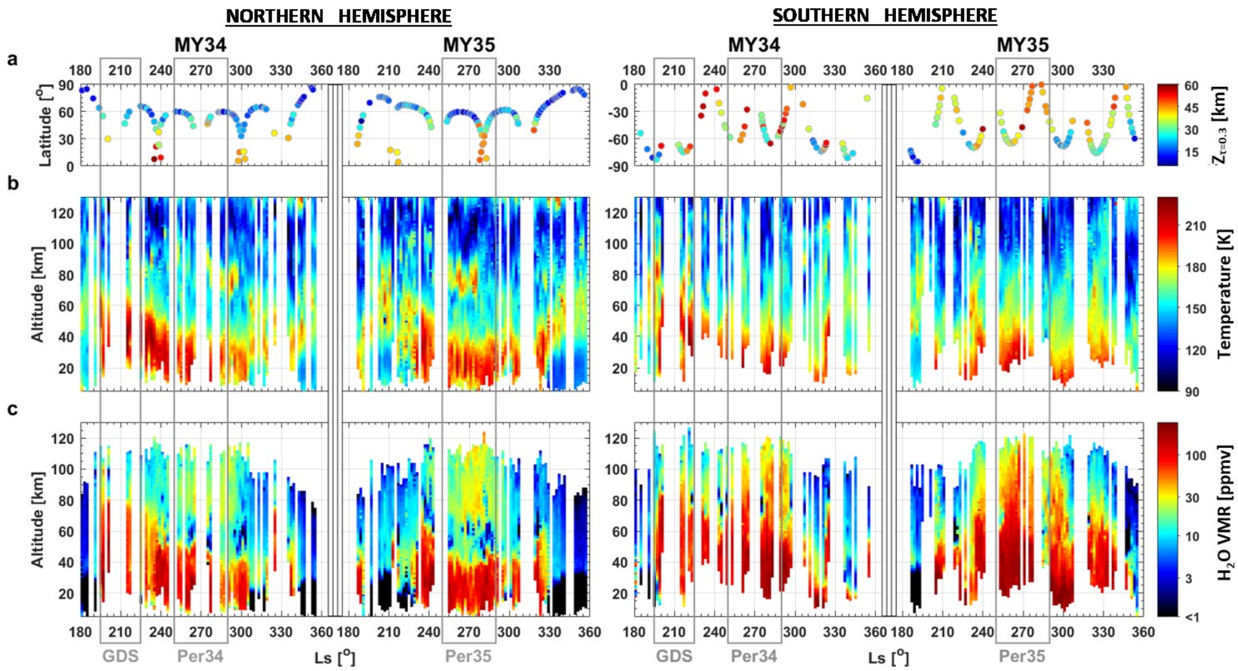

Figure 2. Seasonal map of atmospheric temperature and H_2O mixing ratio during the second half of MY34 and MY35. The data are plotted in function of L_S and altitude for the Northern (left) and the Southern (right) hemispheres. (**a**) Latitudinal distribution of the ACS-MIR solar occultations, depending on an altitude level where the aerosol slant opacity (τ) equals 0.3. (**b**) Temperature. (**c**) Volume mixing ratio (VMR) of water vapor. Grey frames outline time intervals of the global dust storm (GDS) in MY34 and the two perihelions in MY34 (Per34) and MY35 (Per35).

4 H_2O variations around perihelion

To quantify seasonal trends of water content in the mesosphere, we selected three altitude layers corresponding to 80 km, 100 km, and 110–120 km. The first layer, which corresponds to the middle mesosphere, is accessible in all profiles (Fig. 2c) when the vapor concentration exceeds the detection limit of ~10^7 cm^{-3}, even in low water loading periods. Water at 100–120 km shows up only in stormy periods and around perihelion (Fig. 2c).

Observed variations during perihelion for the three selected levels are presented in Figure 3 for both Martian Years. The number of MIR observations at the considered spectral range is low during the dust storm activity of MY34. Nevertheless, a comparison with MY35 reveals significant increases of H_2O mixing ratios during the GDS: by a factor of 6–8 at 80 km (Fig. 3e, 3f) and by a factor of 3–5 at 100-120 km from L_S 190° to 220° (Fig. 3a-3d). Increases at L_S 320°–330° follow annually repeatable dust storm activity at this season, although injecting far less water into the mesosphere than the GDS in MY34. Around Mars perihelion (L_S=240°–300°) water behaves almost identically between MY34 and MY35. For both Martian Years, the maximum H_2O mixing ratio was observed near the Southern summer solstice (L_S~270°), reaching values of 40–80 ppm at 80 km, 30–60 ppm at 100 km, and 20–50 ppm at 110–120 km. In the Northern winter solstice, it varied from 20 to 40 ppm at all levels, 80–120 km. There are groups of points out of general behaviour, i.e. at L_S=270°–280° in Fig. 3, that results from latitudinal variations of the water content (see Fig. S3 in SM). We compare our results at 80 km with the corresponding ACS NIR dataset derived from the MY34 profiles of Fedorova et al. (2020, grey points in Fig. 3e, 3f). The NIR dataset is five times denser than used in the present work, and it observed the H_2O seasonal variations in greater detail, especially during the dust events of MY34.

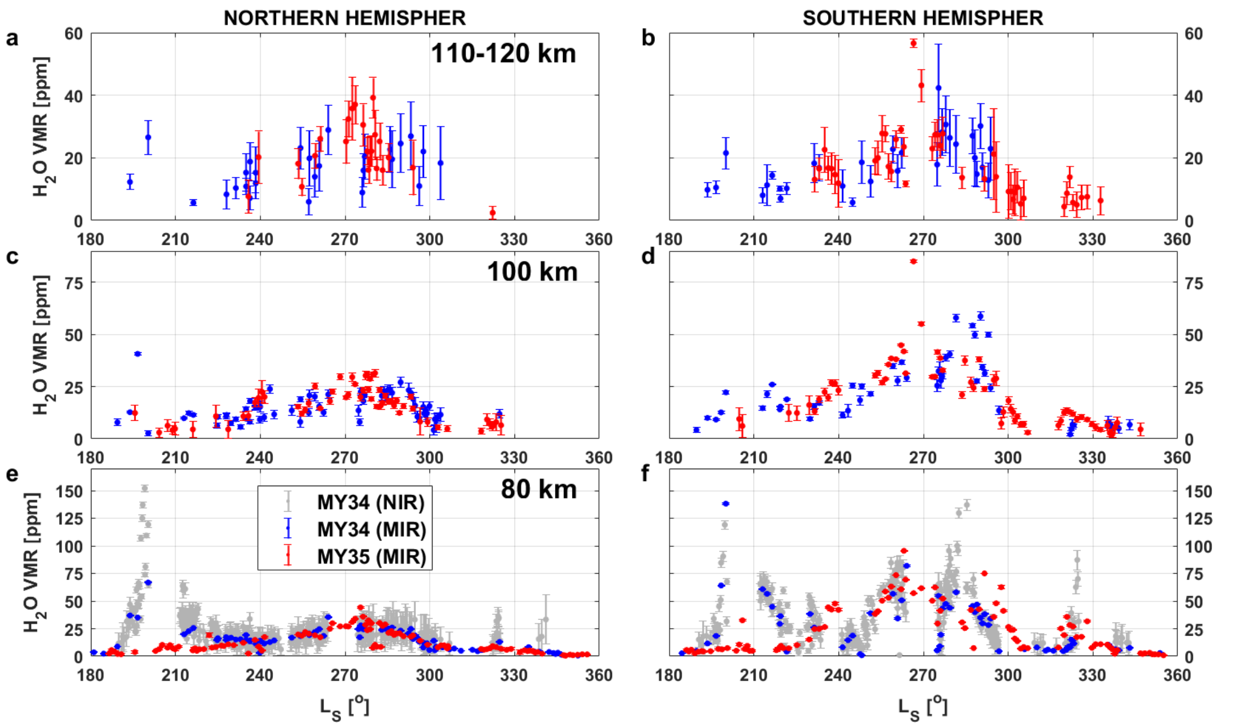

Figure 3. Seasonal trends of H_2O volume mixing ratio (VMR) at three altitude levels: 80, 100, 110-120 km. The season is the second halves of MY34 (in blue) and of MY35 (in red). Each point corresponds to an individual vertical profile: weighted mean value obtained in between 110-120 km (**a, b**), and interpolated value for the levels of 100 km (**c, d**) and 80 km (**e, f**). Data at 80 km in grey (**e, f**) are taken from the ACS NIR profiles (Fedorova et al., 2020).

4 Discussion and Conclusions

For the first time, we report observations of H_2O abundances in a previously unexplored altitude range (from 100 to 120 km). There we find 10–30 ppm of water vapor during the MY34 GDS and 20–50 ppm around Mars perihelions (L_S=250°–290°) of MY34 and MY35 in both hemispheres. Our GDS retrievals at 100–120 km are of the same order of magnitude as MAVEN NGIMS results reported by Stone et al. (2020) at ~150 km. Surprisingly, NGIMS water abundances reveal a 2014-2018 mission-wise maximum of H_2O at 150 km, only during the MY34 GDS, whereas we repeatedly observe the annual maximum around the Southern summer solstice both in MY34 and MY35.

NGIMS measures [H_2O^+] ions, from which neutral H_2O abundances at 150 km were derived on the basis of 1D photochemical modeling. The model was adjusted to reproduce the H_2O VMR at 150 km inferred from the [H_2O^+] ions measured under two scenarios: low water, corresponding to 2 ppm prescribed at 80 km in a non-GDS case; and high water of 40 ppm in a GDS case (Stone et al., 2020; as corrected in March 2021). Notably, all the solar occultation observations performed by TGO and MEX to date (Fedorova et al., 2018, 2020, 2021; Aoki et al., 2019; Villanueva et al., 2021), including the present dataset (Fig. 3e, 3f), report even higher water vapor VMRs at 80 km, of 50–80 ppm during the GDS. Stone et al. (2020) indicate a systematic uncertainty of 69% on their neutral H_2O inference, which is consistent with observed MAVEN, TGO, and MEX values within such error bars.

It is important to consider how ACS's high altitude water vapor abundances combine with photolysis since this process has been hypothesized to be essential, if not the dominant, source for the H atoms observed in the exosphere (Chaffin et al., 2017). The conclusion of Stone et al. (2020) argues for the GDS's predominance and related ion chemistry in the H atoms' production. Our observations suggest that while the GDS period corresponds to the maximum of water abundance at 80 km, H_2O at 120 km peaks only later, at the Southern summer solstice, when it is twice as large as during the GDS. This enhanced solstice maximum suggests that relative water abundance declines more rapidly above 80 km during the GDS than after, during perihelion (Fig. 4).

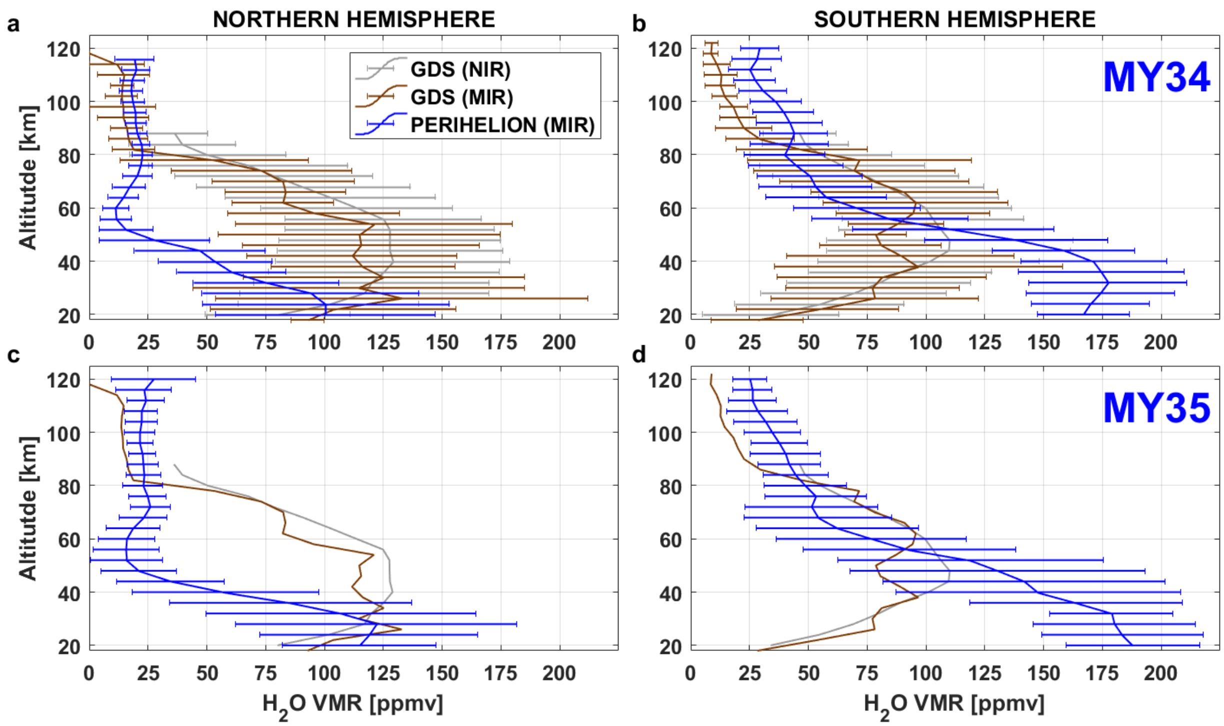

Figure 4. Altitude profiles of average H_2O volume mixing ratio (VMR) during the GDS (MY 34) and the perihelion season (MY 34, 35). The dataset used includes all ACS MIR observations highlighted in Fig. 2: GDS of MY34 (L_S=195°–220°) (brown); the bin around the perihelion point (L_S=250°–295°) (blue). Panels (**a, b**) for MY34 and (**c, d**) for MY35 from the Northern (**a, c**) and Southern (**b, d**) hemispheres. Profiles are presented with 1-sigma dispersion over 4-km altitude bins. Light grey curves are the averages of the NIR data during GDS of MY34 (Fedorova et al., 2020). The GDS curves are also indicated for MY35 to facilitate comparison. For the data points used in the averaging see Fig. S4 of SM.

In Figure 4, we combined altitude profiles from GDS-only (L_S 195°–220°) and perihelion (L_S 250°–295°) intervals to compare averaged vertical trends between them. Here, we also see a coincidence between MIR and NIR GDS profiles in frames of dispersions, which reflect high variability of the observed GDS points (Fig. S4 of SM). The considered H_2O distributions allow estimating an integral escape flux of the atomic hydrogen in each case. For that, we applied the model of Chaffin et al. (2017), which predicts the atmospheric escape rate depending on the water injection into different altitudes (see Figure 3 of their paper). Our rough calculations show that the H escape flux is about ~5×10^9 $cm^{-1}s^{-1}$ during the considered intervals of MY34's GDS and Southern summer solstices of MY 34 and 35. Thus, we claim nearly equivalent contributions from a single GDS and the perihelion period into the hydrogen escape by the high water enrichment in the middle/upper atmosphere. Fedorova et al. (2021) come to a similar conclusion based on SPICAM/MEx water profiles up to 80 km. A GDS occurs every 3–4 martian years on average (Zurek and Martin, 1993; Wang and Richardson, 2015), making the yearly perihelion contribution to the hydrogen escape reasonable. The water enhancements are tied to the circulation regime (Clancy et al., 1996; Richardson and Wilson, 2002; Montmessin et al., 2005). More measurements and modeling would be needed to decide whether the southern summer solstitial transport, currently near perihelion, or the GDS equinoctial circulation prevailed during the history of Mars.

Overall, our results cannot be easily reconciled with water values (up to 60 ppm at 150 km) inferred from NGIMS ion measurements, which suggested that the thermosphere hosted much more water during the GDS than during the rest of the year. However, we note that the only time when Stone et al. (2020) reported measurements around perihelion concerned the L_S interval between 240° and 265° of MY33 (Figure 4 of Stone et al., 2020). It showed the same rough trend as during the onset of the MY34 GDS, with values far exceeding those reported for the regional dust storm of MY33, still a factor of 3 smaller than during the GDS.

Our results remain in line with the conclusion of Fedorova et al. (2020, 2021) that the perihelion season is the primary conveyor of water to high altitudes on a long-term basis. The high values above 100 km fill the gap between the water observed below 100 km and water ions measured by NGIMS at 150 km. Both measurements bring unique constraints in our attempt to understand how the water in the lower atmosphere connects with the escaping hydrogen in the exosphere, an essential step before confidently extrapolating the water escape back in time.

Acknowledgments, Samples, and Data

ExoMars is a joint space mission of the European Space Agency (ESA) and Roscosmos. The ACS experiment is led by the Space Research Institute (IKI) in Moscow, assisted by LATMOS in France. Retrievals and analysis of temperature and water distributions in IKI are funded by grant #20-42-09035 of the Russian Science Foundation. The ACS MIR data are available from ESA's Planetary Science Archive at https://archives.esac.esa.int/psa/#!Table%20View/ACS=instrument. The retrieved data with altitude profiles of H_2O VMR for the considered seasons are available at https://data.mendeley.com/datasets/995y7ymdgm/draft?a=daa72362-898d-4c86-8a13-023b4b59134c.

References

Alday, J., Wilson C. F., Irwin, P. G. J., Olsen, K. S., Baggio, L., Montmessin, F., et al. (2019). Oxygen isotopic ratios in Martian water vapour observed by ACS MIR on board the ExoMars Trace Gas Orbiter. *Astronomy and Astrophysics*, *630*, A91. doi:10.1051/0004-6361/201936234.

Alday, J., Trokhimovskiy, A ., Irwin, P. G. J., Wilson, C. F., Montmessin, F., Lefèvre, F., et al. (2021). Isotopic fractionation of water and its photolytic products in the atmosphere of Mars. *Nature Astronomy* (revised version NATASTRON-20123971B).

Aoki, S., Vandaele, A. C., Daerden, F., Villanueva, G. L., Liuzzi, G., Thomas, I. R., et al. (2019). Water Vapor Vertical Profiles on Mars in Dust Storms Observed by TGO/NOMAD. *Journal of Geophysical Research: Planets*, *124*(12), 3482-3497. doi:10.1029/2019je006109.

Belyaev, D. (2021). Revealing a High Water Abundance in the Upper Mesosphere of Mars with ACS onboard TGO. *Mendeley Data*, v1. http://dx.doi.org/10.17632/995y7ymdgm.1

Benna, M., Mahaffy, P. R., Grebowsky, J. M., Fox, J. L., Yelle, R. V., & Jakosky, B. M. (2015). First measurements of composition and dynamics of the Martian ionosphere by MAVEN's Neutral Gas and Ion Mass Spectrometer. *Geophysical Research Letters*, *42*, 8958–8965, doi:10.1002/2015GL066146.

Chaffin, M., Deighan, J., Schneider, N., & Stewart, A. (2017). Elevated atmospheric escape of atomic hydrogen from Mars induced by high-altitude water. Nature Geoscience, 10(3), 174. doi:10.1038/ngeo2887.

Clancy, R. T., Grossman, A. W., Wolff, M. J., James, P. B., Rudy, D. J., Billawala, Y. N., et al. (1996). Water vapor saturation at low altitudes around Mars aphelion: A key to Mars climate? *Icarus*, *122*(1), 36-62. doi:10.1006/icar.1996.0108.

Clancy, R. T., Smith, M. D., Lefèvre, F., McConnochie, T. H., Sandor, B. J., et al. (2017). Vertical profiles of Mars 1.27 μm O_2 dayglow from MRO CRISM limb spectra: Seasonal/global behaviors, comparisons to LMDGCM simulations, and a global definition for Mars water vapor profiles. *Icarus, 293*, 132-156. doi:10.1016/j.icarus.2017.04.011

Fedorova, A., Bertaux, J.-L., Betsis, D., Montmessin, F., Korablev, O., Maltagliati, L., & Clarke, J. (2018). Water vapor in the middle atmosphere of Mars during the 2007 global dust storm. Icarus, 300, 440–457.

Fedorova, A. A., Montmessin, F., Korablev, O., Luginin, M., Trokhimovskiy, A., Belyaev, D. A., et al. (2020). Stormy water on Mars: The distribution and saturation of atmospheric water during the dusty season. *Science*, *367*(6475), 297-300. doi:10.1126/science.aay9522.

Fedorova, A., Montmessin, F., Korablev, O., Lefèvre, F., Trokhimovskiy, A., & Bertaux, J. L. (2021). Multi-annual monitoring of the water vapor vertical distribution on Mars by SPICAM on Mars Express. *Journal of Geophysical Research: Planets*, *126*, e2020JE006616. doi:10.1029/2020JE006616.

Fox, J. L., Benna, M., Mahaffy, P. R., & Jakosky B. M. (2015). Water and water ions in the Martian thermosphere/ionosphere. *Geophysical Research Letters*, *42*, 8977–8985, doi:10.1002/2015GL065465.

Gamache, R. R., Farese, M., & Renaud, C. L. (2016). A spectral line list for water isotopologues in the 1100–4100 cm-1 region for application to CO_2-rich planetary atmospheres. *Journal of Molecular Spectroscopy*, *326*, 144-150. doi:10.1016/j.jms.2015.09.001.

Gordon, I. E., Rothman, L. S., Hill, C., Kochanov, R. V., Tan, Y., Bernath, P. F., et al. (2017). The HITRAN2016 molecular spectroscopic database. *Journal of Quantum Spectroscopy and Radiative Transfer*, *203*, 3–69. doi:10.1016/j.jqsrt.2017.06.038.

Heavens, N. G., Kleinböhl, A., Chaffin, M. S., Halekas, J. S., Kass, D. M., Hayne, P. O., et al. (2018). Hydrogen escape from Mars enhanced by deep convection in dust storms. *Nature Astronomy*, *2*(2), 126-132. doi:10.1038/s41550-017-0353-4.

Heavens, N. G., Kass, D. M., & Shirley, J. H. (2019). Dusty deep convection in the mars year 34 planet-encircling dust event. *Journal of Geophysical Research: Planets, 124*(11), 2863–2892. https://doi.org/10.1029/2019JE006110.

Jakosky, B. M. (1985). The seasonal cycle of water on Mars. *Space Science Review*, *41*, 131–200. doi:10.1007/BF00241348.

Korablev, O. I., Montmessin, F., Trokhimovskiy, A., Fedorova, A. A., Shakun, A. V., Grigoriev, A. V., et al. (2018). The Atmospheric Chemistry Suite (ACS) of Three Spectrometers for the ExoMars 2016 Trace Gas Orbiter. *Space Science Review*, *214*(1). doi:10.1007/s11214-017-0437-6

Krasnopolsky, V. A. (2002). Mars' upper atmosphere and ionosphere at low, medium, and high solar activities: implications for evolution of water. *Journal of Geophysical Research*, *107*(E12), 5128. doi:10.1029/2001JE001809.

Krasnopolsky, V. A. (2015). Variations of the HDO/H2O ratio in the martian atmosphere and loss of water from Mars. *Icarus*, *257*, 377–386. doi:10.1016/j.icarus.2015.05.021.

Krasnopolsky, V. A. (2019). Photochemistry of water in the martian thermosphere and its effect on hydrogen escape. *Icarus*, *321*, 62–70. doi:10.1016/j.icarus.2018.10.033.

Malathy Devi, V., Benner, D. C., Sung, K., Crawford, T. J., Gamache, R. R., Renaudc, C. L., et al. (2017). Line parameters for CO_2- and self-broadening in the ν3 band of $HD^{16}O$. *Jouranal of Quantum Spectroscopy and Radiative Transfer*, *203*, 158–174. doi:10.1016/j.jqsrt.2017.02.020.

Maltagliati, L., Montmessin, F., Korablev, O., Fedorova, A., Forget, F., Määttänen, A., Lefèvre, F., & Bertaux, J.-L. (2013). Annual survey of water vapor vertical distribution and water–aerosol coupling in the martian atmosphere observed by SPICAM/MEx solar occultations. *Icarus*, *223*, 942–962. doi:10.1016/j.icarus.2012.12.012.

Marquardt, D. (1963). An Algorithm for Least-Squares Estimation of Nonlinear Parameters". SIAM. *Journal on Applied Mathematics*, *11*(2), 431–441. doi:10.1137/0111030.

Millour, E., Forget, F., Spiga, A., Vals, M., Zakharov, V., Montabone, L., et al. (2018). *The Mars Climate Database (version 5.3)*. Paper presented at the Mars Science Workshop "From Mars Express to ExoMars", held 27-28 February 2018 at ESAC, Madrid, Spain, id.68. https://www.cosmos.esa.int/web/mars-science-workshop-2018.

McElroy, M. B., & Donahue, T. M. (1972). Stability of the Martian atmosphere. *Science*, *177*(4053), 986-8 986. doi:10.1126/science.177.4053.986.

Montabone, L., Spiga, A., Kass, D. M., Kleinböhl, A., Forget, F., & Millour, E. (2020). Martian Year 34 column dust climatology from Mars Climate Sounder observations:

Reconstructed maps and model simulations. *Journal of Geophysical Research: Planets*, *125*(8), e06111. doi:10.1029/2019JE006111.

Montmessin, F., Fouchet, T., & Forget, F. (2005). Modeling the annual cycle of HDO in the Martian atmosphere. *Journal of Geophysical Research: Planets, 110*, E03006. doi:10.1029/2004JE002357

Neary, L., Daerden, F., Aoki, S., Whiteway, J., Clancy, R., Smith, M., et al. (2020). Explanation for the increase in high-altitude water on Mars observed by NOMAD during the 2018 global dust storm. *Geophysical Research Letters, 47*(7), e2019GL084354. https://doi.org/10.1029/2019GL084354.

Owen, T., Maillard, J. P., de Bergh, C., & Lutz, B. L. (1988). Deuterium on Mars: The abundance of HDO and the value of D/H. *Science*, *240*, 1767–1770. doi:10.1126/science.240.4860.1767.

Richardson, M. I., & Wilson, R. J. (2002). Investigation of the nature and stability of the Martian seasonal water cycle with a general circulation model. *Journal of Geophysical Research*, *107*(E5), 5031, doi:10.1029/2001JE001536.

Rodin, A. V., Korablev, O. I., & Moroz, V. I. (1997). Vertical distribution of water in the near-equatorial troposphere of Mars: water vapor and clouds. *Icarus*, *125*(1), 212-229. doi:10.1006/icar.1996.5602.

Rossi, L., Vals, M., Montmessin, F., Forget, F., Millour, E., Fedorova, A., Trokhimovskiy, A., & Korablev, O., (2021). The Effect of the Martian 2018 Global Dust Storm on HDO as Predicted by a Mars Global Climate Model. *Geophysical Research Letters, 48*(7), https://doi.org/10.1029/2020GL090962.

Shaposhnikov, D. S., Medvedev, A. S., Rodin, A. V., & Hartogh, P. (2019). Seasonal water “pump” in the atmosphere of mars: Vertical transport to the thermosphere. *Geophysical Research Letters*, *46*, 4161–4169. doi:10.1029/2019GL082839.

Stone, W., Yelle, R. V., Benna, M., Lo, D. Y., Elrod, M. K., & Mahaffy P. R. (2020). Hydrogen escape from Mars is driven by seasonal and dust storm transport of water. *Science*, *370*(6518), 824–831. doi:10.1126/science.aba5229.

Villanueva, G. L., Liuzzi, G., Crismani, M. M. J., Aoki, S., Vandaele, A. C., et al. (2021). Water heavily fractionated as it ascends on Mars as revealed by ExoMars/NOMAD. *Science Advances, 7*(7), eabc8843. doi:10.1126/sciadv.abc8843.

Wang, H., & Richardson, M. I. (2015). The origin, evolution, and trajectory of large dust storms on Mars during Mars years 24-30 (1999-2011). *Icarus*, *251*, 112-127. doi:10.1016/j.icarus.2013.10.033.

Zurek, R. W. & Martin, L. J. (1993). Interannual variability of planet-encircling dust storms on Mars. *Journal of Geophysical Research*, *98*(E2), 3247-3259. doi:10.1029/92JE02936.

Geophysical Research Letters

Supporting Information for

Revealing a High Water Abundance in the Upper Mesosphere of Mars with ACS onboard TGO

Denis A. Belyaev[1], Anna A. Fedorova[1], Alexander Trokhimovskiy[1], Juan Alday[2], Franck Montmessin[3], Oleg I. Korablev[1], Franck Lefèvre[3], Andrey S. Patrakeev[1], Kevin S. Olsen[2], and Alexey V. Shakun[1]

[1]Space Research Institute (IKI), Moscow, Russia.

[2]Department of Physics, University of Oxford, UK.

[3]LATMOS/CNRS, Paris, France.

Corresponding author: Denis Belyaev (dbelyaev@iki.rssi.ru)

Contents of this file

Introduction

The present Supporting Information describes details of the ACS MIR instrument and the concept of altitude profiles retrievals from the measured transmission spectra. The retrieval algorithm is supplemented by Figure S1, which demonstrates instrumental and temperature peculiarities of the CO_2 and H_2O absorption spectroscopy around 2.7 μm band (echelle order #223 of ACS MIR). Figure S2 shows validation of the derived temperature, H_2O number density and mixing ratio profiles for different seasonal scenarios in MY34. Latitudinal variation of the high altitude water around perihelion is presented in Figure S3 for both MY34 and MY35. Figure S4 presents vertical distribution of all data points for H_2O VMR in the GDS and perihelion seasons. Uncertainties of the obtained data are described separately in section Text S3.

Text S1. Instrument description

The middle infrared channel of the Atmospheric Chemistry Suite is a cross-dispersion echelle spectrometer dedicated to solar occultation measurements in the 2.3–4.3 μm wavelength range (Korablev et al., 2018). Each occultation session is devoted to one of ten angular positions of the MIR secondary grating that disperses about 10-20 echelle orders spatially separated and recorded simultaneously at the focal plane array (FPA) by 640x512 pixels. The spectral range of our interest, 2.66-2.68 μm, lies within the diffraction order #223 at the grating position #4. One order covers a spectral interval of about 30 cm^{-1} (~25 nm); a spectrum is dispersed along 640 FPA elements with the sampling of 0.05 cm^{-1} and the resolving power λ/δλ reaching ~25000 (δλ~0.15 cm^{-1}). In the occultation field of view (FOV), the instrumental rectangular slit cuts a part from the solar disk, so that one order occupies a stripe with about 20 FPA rows. In such a manner, the consequences of orders are located on the matrix as stripe-by-stripe, one above the other, with some dark rows between them. For our analysis, we selected a central row from the stripe correspondent to order #223 that provides the maximal signal-to-noise ratio.
The calibration procedure for the analyzed transmissions encompassed a pixel-to-wavenumber assignment and a determination of the instrument line shape (ILS). The procedure was applied for every occultation and in various spectral intervals separately since we observed variability of the light spreading over the FPA from orbit to orbit. Using strong CO_2 and H_2O absorption lines in order #223, we derived an optimal wavenumber assignment by a parabolic law and an asymmetric ILS including a superposition of two Gaussian functions (Fig. S1a). Previously, Alday et al. (2019) implemented an analogous approach for MIR spectra but in the grating position #5.

Text S2. Retrieval concept

A scheme for the water VMR retrieval consists of several iterations with a fitting of a forwardly modeled transmission spectrum to a measured one at each observed altitude. The forward modeling includes contributions from H_2O, HDO, and CO_2 molecular absorption cross-sections that are abundant in the 2.66-2.68 μm spectral range, i.e. 3730-3755 cm^{-1} (Fig. S1b). They were calculated using line-by-line modeling for specified temperatures and pressures on a basis of the HITRAN2016 database (Gordon et al., 2017) taking into account H_2O and HDO lines broadening in the CO_2-rich atmosphere (Gamache et al., 2016; Malathy Devi et al., 2017) and self-broadening in the case of CO_2. A transmission spectrum $J(\nu,T,p)$ is defined by the cross-sections $\sigma(\nu,T,p)$, gaseous concentrations $N_{mol} = f_{mol} \bullet p/k_B T$, and aerosol slant opacity τ_a. Here, ν is wavenumber; T and p are the atmospheric temperature and pressure respectively; f_{mol} – volume mixing ratio (VMR) of a molecule; k_B – Boltzmann constant. In order to fit such a synthetic spectrum J_{mod} to the measured one J_{mes}, we convolved the model by the previously derived ILS using wavenumber calibrations. The aerosol opacity $\tau_a = -log(J_a)$ was fitted from the measured transmission as a continuum level J_a out of molecular absorption.
The fitting procedure includes minimization of the function $\chi^2 = \sum_i A^2(\nu_i)$, which is a residuals sum over all considered spectral points i (pixels) divided by the transmission errors $\delta J(\nu_i)$, where $A(\nu_i) = \left(J_{mod}(\nu_i) - J_{mes}(\nu_i)\right)/\delta J(\nu_i)$. An optimal search for the minimum was based on Levenberg-Marquardt algorithm (Marquardt, 1963) with the Jacobian matrix containing transmission derivatives [$\partial A/\partial X$] on free parameters X, i.e. T, N_{CO_2}, f_{H_2O} or τ_a. Here, the clue contribution comes from the partial cross-section derivative on temperature $\partial\sigma/\partial T$. It differs for each molecule from line to line with a change of sign as seen in the Figure S1c. Thanks to that, an independent and simultaneous retrieval of temperature and molecular concentrations is possible.

In our multi iteration scheme, the first step is devoted to temperature and pressure retrievals with the rotational structure of CO_2 absorption bands. They are selected out from strong H_2O and HDO lines, e.g. in intervals 3733-3735 cm^{-1}, 3738-3743 cm^{-1} of the order #223. Total number of spectral points exceeds 150 that makes the χ^2-minimization confidential. Altitude profiles $T_1(z)$ and $N_{CO2}(z)$ are directly retrieved, while the pressure is expressed on the first stage through the ideal gas law as $p_1(z) = \left({N_{CO2}(z)}\middle/{f_{CO2}(z)}\right) k_B T_1(z)$. The CO_2 VMR vertical distribution $f_{CO2}(z)$ is taken from the Mars Climate Database (MCD) (Millour et al., 2018). Then, in order to meet the hydrostatic law, we constrain the pressure by a formula for the hydrostatic equilibrium, $p_{hyd}(z) = p_o exp\left[-\int_{z_o}^{z} \frac{g(h)M(h)}{k_B T_1(h)} dh\right]$, using the retrieved $T_1(z)$. Here, g is the gravity acceleration, M is the molecular weight (taken from MCD). A reference pressure $p_o = p(z_o)$ is selected at an altitude z_o, where the retrieval uncertainties are minimal. In all derived profiles, this level lies between 30 and 60 km corresponding to the deepest, but not saturated, absorption lines (see Fig. 1b). Once the hydrostatic pressure profile is calculated, we keep it fixed when a new temperature and CO_2 density are retrieved on the next step. We repeat this procedure about 4-5 iterations reaching the profiles convergence. Values on an (i-1)th step are used as a priori for the ith one, while for the 1st stage we take the values from MCD. Analogous hydrostatic approach has been recently verified by other temperature and pressure retrievals from the ACS data (Alday et al., 2019, 2021; Fedorova et al., 2020). On the last stage, we apply the temperature and density profiles as a reference atmosphere for the H_2O mixing ratio retrieval (Fig. S2c) in the wavenumber interval from 3743 to 3753 cm^{-1}. We do not fit the HDO concentration separately and keep it as 5 times of the terrestrial SMOW value (Standard Mean Ocean Water), which is $1.56 \bullet 10^{-4}$ for this isotope (Owen et al., 1988; Krasnopolsky, 2015). This assumption simplifies the fit, decreasing the number of free parameters, and it makes sense for the tiny detection of high altitude water. In parallel, each retrieval is accompanied by the derived aerosol opacity τ_a, which may characterize the dust activity during an occultation (see Figure 2a).

Examples of the derived temperature, H_2O number density and mixing ratio profiles are shown on Figure S2 in comparison with collocated and simultaneous occultations by the ACS near-IR channel (see in Fedorova et al. (2020)), as well as with the MCD predictions for particular occultations. The validation is demonstrated for three orbits that correspond to different atmospheric scenarios in MY34: before GDS (L_S 164°), during GDS (L_S 196.6°) and close to perihelion (L_S 260.9°). Sensitivity of the NIR spectroscopy does not allow measuring temperature and densities above 100 km. In the MIR case, one can potentially retrieve the temperature altitude profiles spreading from 10-40 km (depending on aerosol opacity) up to 150 km in the considered spectral range (Fig. S2a). The upper altitude of the water detection is 20-25 km higher for the 2.66-2.67 µm band in MIR than 1.38 µm in NIR (Fig. S2b, S2c).

Text S3. Estimation of uncertainties

The transmission errors δJ, included in the Jacobian matrix, determine uncertainties of the retrievals for each of free parameters. We estimated them for any observed altitude as a multiplication of the derivatives array by the transposed one, $\delta X = \sqrt{[\frac{\partial A}{\partial X}] \times [\frac{\partial A}{\partial X}]'}$, over the spectral points. The error bars δJ are composed of a statistical noise and some systematic uncertainties. We derived the statistical noise analyzing transmission fluctuations near 1 at altitudes above 200 km. It gave the standard deviation of about $5 \bullet 10^{-4}$ for a signal recorded in the considered FPA row and in the center of the range, 3735-3750 cm^{-1}. The systematics comes from the obtained calibrations (wavenumber, ILS) and from the hydrostatic pressure and temperature uncertainties when modeling transmission spectra on the final step of H_2O VMR retrievals. On average, it increases the δJ value up to 0.001-0.0015. The described uncertainties establish a detection limit of $5•10^6$-$1•10^7$ cm^{-3} for H_2O number density above 100 km. When the water enrichment exceeds this order of magnitude, we observe a positive detection of the molecular abundance at high altitudes. In the opposite case, an upper limit is determined (see Fig. 1c).

Supplementing Figures:

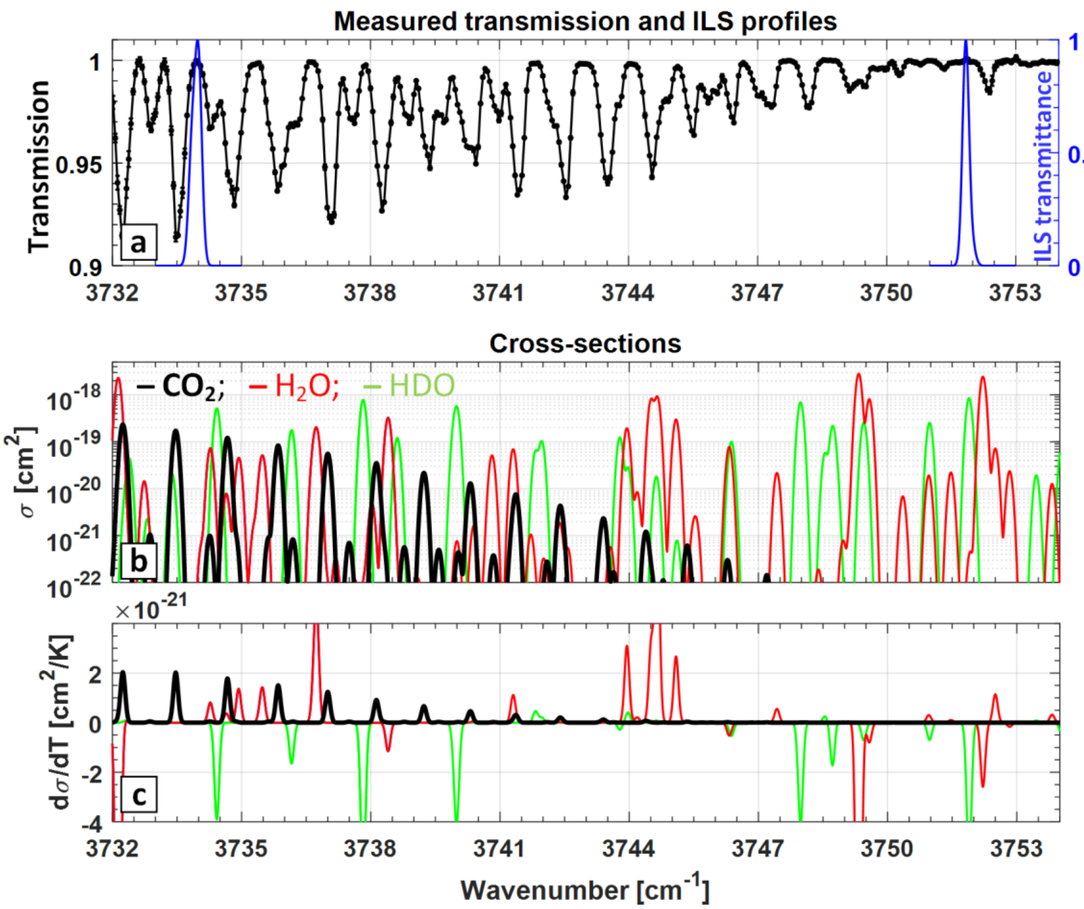

Figure S1. Absorption spectroscopy in the echelle order #223 of ACS MIR. **a**: Example of measured transmission spectrum at a target altitude of 100 km (black axis) and the instrumental line shape (ILS) for both edges of the considered wavenumber range (blue axis). **b**: Absorption cross-sections for molecules CO_2 (black), H_2O (red), and HDO (green) calculated for T=150 K and p=10^{-5} mbar and convolved by ILS. **c**: Partial temperature derivatives of the considered cross-sections.

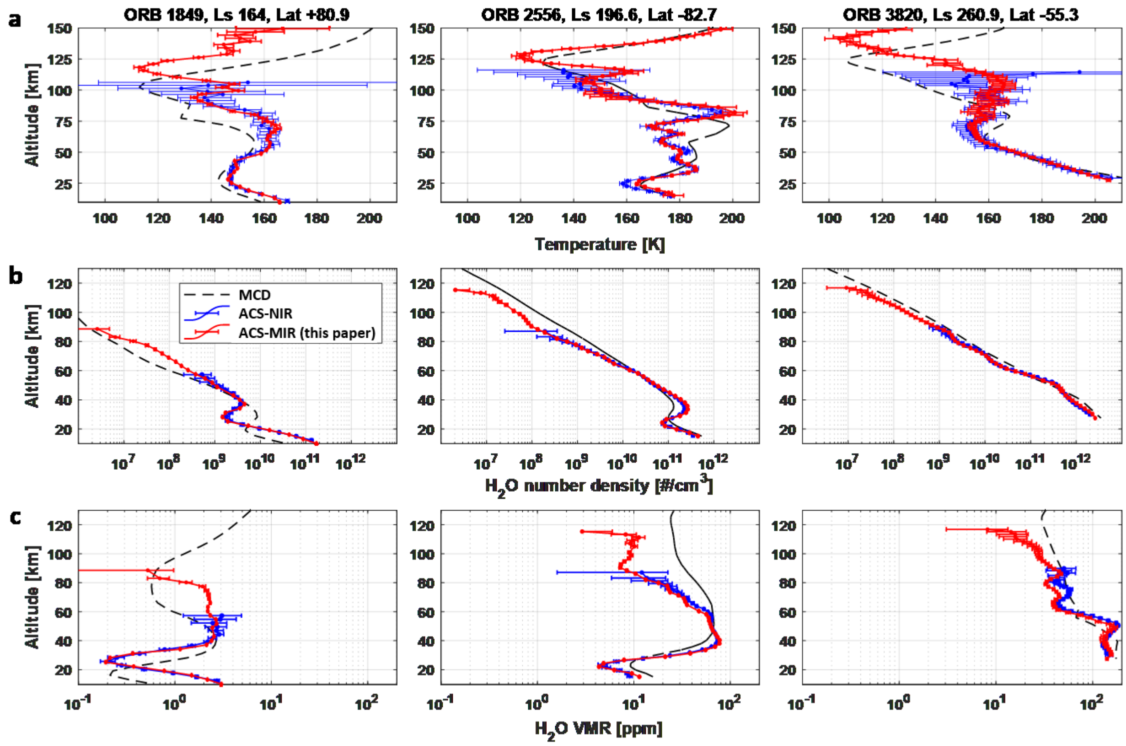

Figure S2. Validation of vertical profiles retrieved by ACS-MIR (red) with analogous profiles of ACS-NIR (from Fedorova et. al, 2020) (blue) and with predictions of MCD (Millour et al., 2018) (black): (**a**) temperature; (**b**) H_2O number density; (**c**) H_2O volume mixing ratio (VMR).

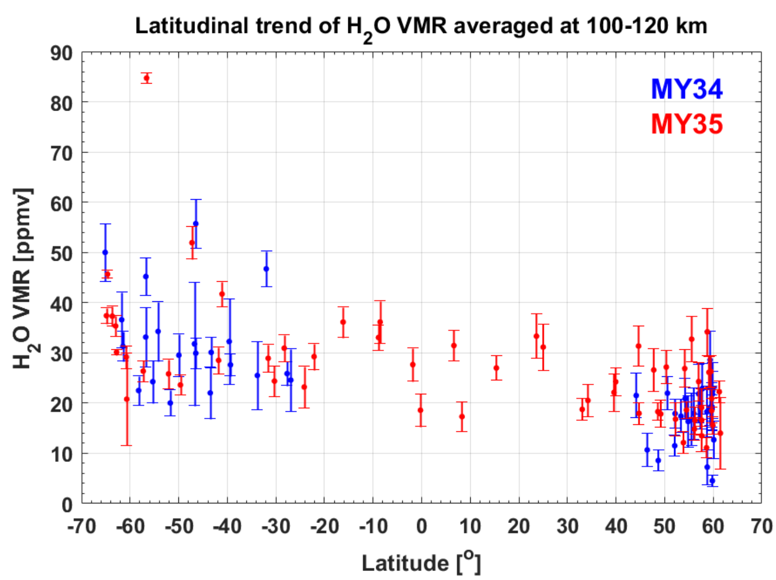

Figure S3. Latitudinal trend of H2O volume mixing ratio (VMR) in the perihelion seasons (Ls 250°–295°) of MY34 (blue) and MY35 (red). Each individual point is a weighted mean value revealed over altitude range of 100-120 km from a vertical profile of water VMR.

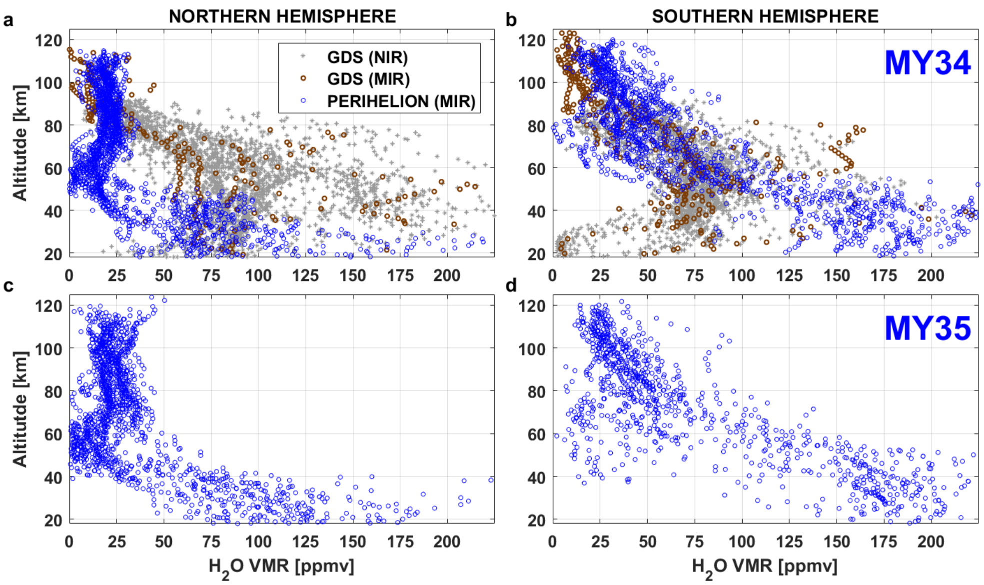

Figure S4. Altitude distribution of H_2O volume mixing ratio (VMR) during the GDS (MY 34) and the perihelion season (MY 34, 35). The dataset used includes all ACS MIR observations at GDS of MY34 (L_S=195°–220°) (brown) and around the perihelion point (L_S=250°–295°) (blue). Panels (a, b) for MY34 and (c, d) for MY35 from the Northern (a, c) and Southern (b, d) hemispheres. Light grey points are the NIR data during GDS of MY34 (Fedorova et al., 2020).